

Long-wavelength optical coherence tomography at 1.7 μm for enhanced imaging depth

Utkarsh Sharma, Ernest W. Chang, and Seok H. Yun*

Harvard Medical School and Wellman Center for Photomedicine, Massachusetts General Hospital,
40 Blossom Street, Boston, MA 02114, USA

*Corresponding author: svun@hms.harvard.edu

Abstract: Multiple scattering in a sample presents a significant limitation to achieve meaningful structural information at deeper penetration depths in optical coherence tomography (OCT). Previous studies suggest that the spectral region around 1.7 μm may exhibit reduced scattering coefficients in biological tissues compared to the widely used wavelengths around 1.3 μm . To investigate this long-wavelength region, we developed a wavelength-swept laser at 1.7 μm wavelength and conducted OCT or optical frequency domain imaging (OFDI) for the first time in this spectral range. The constructed laser is capable of providing a wide tuning range from 1.59 to 1.75 μm over 160 nm. When the laser was operated with a reduced tuning range over 95 nm at a repetition rate of 10.9 kHz and an average output power of 12.3 mW, the OFDI imaging system exhibited a sensitivity of about 100 dB and axial and lateral resolution of 24 μm and 14 μm , respectively. We imaged several phantom and biological samples using 1.3 μm and 1.7 μm OFDI systems and found that the depth-dependent signal decay rate is substantially lower at 1.7 μm wavelength in most, if not all samples. Our results suggest that this imaging window may offer an advantage over shorter wavelengths by increasing the penetration depths as well as enhancing image contrast at deeper penetration depths where otherwise multiple scattered photons dominate over ballistic photons.

©2008 Optical Society of America

OCIS codes: (110.4500) Optical coherence tomography; (140.3600) Lasers, tunable; (170.3660) Light propagation in tissues; (170.3880) Medical and biological imaging.

References and links

1. J. M. Schmitt, "Optical coherence tomography (OCT): A review," *IEEE J. Sel. Top. Quantum Electron.* **5**, 1205-1215 (1999).
2. J. M. Schmitt, A. Knuttle, M. J. Yadlowsky, and M. A. Eckhaus, "Optical coherence tomography of dense tissue: statistics of attenuation and backscattering," *Phys. Med. Biol.* **39**, 1705-1720 (1994).
3. L. Thrane, H. T. Yura, and P. E. Anderson, "Analysis of optical coherence tomography systems based on extended Huygens-Fresnel principle," *J. Opt. Soc. Am. A* **17**, 484-494 (2000).
4. M. J. Yadlowsky, J. M. Schmitt, and R. F. Bonner, "Multiple scattering in optical coherence microscopy," *Appl. Opt.* **34**, 5699-5707 (1995).
5. Y. T. Pan, R. Birngruber, and R. Engelhardt, "Contrast limits of coherence-gated imaging in scattering media," *Appl. Opt.* **36**, 2979-2983 (1997).
6. R. K. Wang, "Signal degradation by multiple scattering in optical coherence tomography of dense tissue: a Monte Carlo study towards optical clearing of biotissues," *Phys. Med. Biol.* **47**, 2281-2299 (2002).
7. J. M. Schmitt and A. Knuttle, "Model of optical coherence tomography of heterogenous tissue," *J. Opt. Soc. Am. A* **14**, 1231-1242 (1997).
8. S. G. Adie, T. R. Hillman, and D. D. Sampson, "Detection of multiple scattering in optical coherence tomography using the spatial distribution of Stokes vectors," *Opt. Express* **15**, 18033-18049 (2007), <http://www.opticsinfobase.org/abstract.cfm?URI=oe-15-26-18033>.
9. G. Yao and L. V. Wang, "Monte Carlo simulation of an optical coherence tomography signal in homogeneous turbid media," *Phys. Med. Biol.* **44**, 2307-2320 (1999).
10. L. Thrane, M. B. Frosz, T. M. Jorgensen, A. Tycho, H. T. Yura, and P. E. Anderson, "Extraction of optical scattering parameters and attenuation compensation in optical coherence tomography images of multilayered tissue structures," *Opt. Lett.* **29**, 1641-1643 (2004).

11. V. V. Tuchin, I. L. Maksimova, D. A. Zimnyakov, I. L. Kon, A. H. Mavlutov, and A. A. Mishin, "Light propagation in tissues with controlled optical properties," *J. Biomed. Opt.* **2**, 401–417 (1997).
12. R. K. Wang and X. Xu, "Concurrent enhancement of imaging depth and contrast for optical coherence tomography by hyperosmotic agents," *J. Opt. Soc. Am. B* **18**, 948–953 (2001).
13. M. E. Brezinski, G. J. Tearney, B. E. Bouma, J. A. Izatt, M. R. Hee, E. A. Swanson, J. F. Southern, and J. G. Fujimoto, "Optical coherence tomography for optical biopsy," *Circulation* **93**, 1206-1213 (1996).
14. Y. Pan and D. L. Farkas, "Noninvasive imaging of living human skin with dual-wavelength optical coherence tomography in two and three dimensions," *J. Biomed. Opt.* **3**, 446-455 (1998).
15. A. Unterhuber, B. Považay, B. Hermann, H. Sattmann, A. Chavez-Pirson, and W. Drexler, "In vivo retinal optical coherence tomography at 1040 nm - enhanced penetration into the choroid," *Opt. Express* **13**, 3252-3258 (2005), <http://www.opticsinfobase.org/abstract.cfm?URI=oe-13-9-3252>.
16. E. C. Lee, J. F. de Boer, M. Mujat, H. Lim, and S. H. Yun, "In vivo optical frequency domain imaging of human retina and choroid," *Opt. Express* **14**, 4403-4411 (2006), <http://www.opticsinfobase.org/abstract.cfm?URI=oe-14-10-4403>.
17. B. E. Bouma, L. E. Nelson, G. J. Tearney, D. J. Jones, M. E. Brezinski, and J. G. Fujimoto, "Optical coherence tomographic imaging of human tissue at 1.55 μm and 1.81 μm using Er- and Tm-doped fiber sources," *J. Biomed. Opt.* **3**, 76-79 (1998).
18. N. Nishizawa, Y. Chen, P. Hsiung, E. P. Ippen, and J. G. Fujimoto, "Real-time, ultrahigh-resolution, optical coherence tomography with an all-fiber, femtosecond fiber laser continuum at 1.5 μm ," *Opt. Lett.* **29**, 2846-2848 (2004).
19. T. L. Troy and S. N. Thennadil, "Optical properties of human skin in the near infrared wavelength range of 1000 to 2200 nm," *J. Biomed. Opt.* **6**, 167-176 (2001).
20. A. N. Bashkatov, E. A. Genina, V. I. Kochubey, and V. V. Tuchin, "Optical properties of the subcutaneous adipose tissue in the spectral range 400-2500 nm," *Opt. Spectrosc.* **99**, 836-842 (2005).
21. G. M. Hale and M. R. Querry, "Optical constants of water in the 200 nm to 200 μm wavelength region," *Appl. Opt.* **12**, 555-563 (1973).
22. L. Kou, D. Labrie, and P. Chylek, "Refractive indices of water and ice in the 0.65 – 2.5 μm spectral range," *Appl. Opt.* **32**, 3531-3540 (1993).
23. S. H. Yun, C. Boudoux, G. J. Tearney, and B. E. Bouma, "High-speed wavelength-swept semiconductor laser with a polygon-scanner-based wavelength filter," *Opt. Lett.* **28**, 1981-1983 (2003).
24. S. H. Yun, G. J. Tearney, J. F. de Boer, N. Iftima, and B. E. Bouma, "High-speed optical frequency-domain imaging," *Opt. Express* **11**, 2953-2963 (2003), <http://www.opticsinfobase.org/abstract.cfm?URI=oe-11-22-2953>.
25. S. H. Yun, G. J. Tearney, B. J. Vakoc, M. Shishkov, W. Y. Oh, A. E. Desjardins, M. J. Suter, R. C. Chan, J. A. Evans, I. K. Jang, N. S. Nishioka, J. F. de Boer, and B. E. Bouma, "Comprehensive volumetric optical microscopy in vivo," *Nat. Med.* **12**, 1429-1433 (2006).
26. J. M. Schmitt, A. Knuttle, and R. F. Knuttle, "Measurement of optical properties of biological tissues by low coherence interferometry," *Appl. Opt.* **32** 6032-6042 (1993).
27. B. W. Colston Jr, M. J. Everett, U. S. Sathyam, L. B. DaSilva, and L. L. Otis, "Imaging of the oral cavity using optical coherence tomography," *Assessment of Oral Health, Monographs in Oral Science, R. V. Faller, ed., (Basel, Karger, 2000), vol 17, pp 32-55.*

1. Introduction

Optical coherence tomography (OCT) is a high-resolution imaging technique that is actively used for various biomedical applications, such as medical diagnosis. This technique provides cross-sectional images of biological tissues over penetration depths of typically 1 to 3 mm. Although OCT is a unique and useful imaging modality, the relatively shallow penetration depth is considered a serious limitation for many applications [1]. The image formation of OCT relies on the measurement of backscattered photons from various depths and scattering sites in the tissue. These photons could be classified into least scattered or singly-reflected ballistic photons, and multiple scattered photons [2,3]. Singly scattered photons contribute to the meaningful OCT signal, while multiple scattered photons essentially add to the background noise. The penetration depth of OCT is fundamentally limited by the attenuation of ballistic light propagation via scattering and absorption. Besides the scattering and absorption losses, the phenomenon of multiple scattering also makes it difficult to achieve meaningful structural information at deeper penetration depths [4]. The fraction of multiply-scattered photons that contributes to the OCT image increases with the depth (optical delay) in tissue, resulting in reduced signal localization (both lateral and longitudinal) and decreased image contrast at larger depths [4-6]. While scattering is the major contrast mechanism in

OCT, a reduction of light scattering in a sample may actually increase the penetration depth and contrast in the image.

Several theoretical and experimental studies have been conducted to get insights into the phenomenon of multiple scattering in tissues and its detrimental effects on OCT imaging [2,4,6-8]. Monte Carlo simulation has been used to study and ultimately compensate for the effect of multiple scattering. However, this approach has been limited to samples involving homogeneous media or layered tissues with simple geometry [3,9,10]. Post-processing correction of multiple scattering has been ineffective without knowing *a priori* the detailed optical properties of heterogeneous tissues. Optical clearing, a method involving chemical administration (such as glycerol and dimethyl sulfoxide), can enhance penetration depth by reducing optical scattering in tissues [11,12] and may be used in limited applications.

Optical properties of tissues tend to vary significantly as a function of wavelength; therefore, an optimal spectral window may be chosen for maximizing light penetration and enhancing image contrast at deeper depths. A clear improvement in the penetration depth was demonstrated by using 1.3 μm versus 0.85 μm OCT systems [13,14] and using 1.06 μm over 0.85 μm in the retina [15,16]. OCT systems at 1.55 μm and 1.8 μm have also shown comparable penetration depth to that of 1.3 μm systems [17,18]. Other studies suggested that scattering coefficients of bulk skin and adipose tissues are $\sim 20\%$ lower at 1.7 μm compared to 1.3 μm [19,20]. Optical absorption by water content ($\sim 70\%$) in a biological tissue causes a propagation loss of 2-3 dB/mm around the wavelength of 1.7 μm , which in fact is less than the loss caused by Rayleigh and Mie scattering. However, the water absorption loss increase significantly at around 1.5 μm and beyond 1.85 μm [21,22]. The inferences drawn from these studies suggest that the spectral window of 1.6-1.8 μm could provide optimal performance for enhancing image contrast at larger penetration depths. However, this remains controversial, to the best of our knowledge.

In this paper, we describe an experimental investigation of the long-wavelength window for OCT imaging. For this study, we develop a wavelength swept laser and realize swept-source OCT or optical frequency domain imaging (OFDI), for the first time in the 1.7 μm spectral range. We image several phantom and biological samples using the 1.7- μm OFDI system and compare the images directly with those obtained from a state-of-the-art 1.3- μm OFDI system with similar sensitivity and resolution. We show that the spectral range around 1.7 μm is a promising window for OCT imaging.

2. Experimental setup: Design and system characteristics

2.1 Wavelength swept laser: Design and laser output characteristics

Figure 1 shows a schematic of the swept laser, which employs a semiconductor optical amplifier (SOA) with a nominal center wavelength of 1700 nm (Covega) in a linear extended cavity. The SOA chip has dielectric coating for high reflection (HR: $\sim 90\%$) on one side that serves as a cavity feedback mirror, and anti-reflection coating on the other side. Diverging emission from the SOA chip was collimated using an aspheric lens ($f = 4.5\text{mm}$). We used a rotating polygon-based scanning filter previously developed [23]. We implemented two different filter designs, 1 and 2. Design 1 was used to obtain the maximum possible tuning range offered by the gain bandwidth of the SOA. Design 2 was chosen to produce a reduced tuning range so that OFDI can be performed at an optimized sensitivity using an existing InGaAs detector available in our laboratory. We note that extended InGaAs material can cover the spectral range from 1.2 to 2.6 μm . The filter comprised of a diffraction grating (600 g/mm, Edmund Optics), a telescope (Design 1: $f_1 = 45$ mm, $f_2 = 45$ mm; Design 2: $f_1 = 150$ mm, $f_2 = 50$ mm), and a polygon scanning mirror (Lincoln Lasers, Design 1: 72 facets, Design 2: 36 facets). A pellicle beam splitter (45R/55T, Thorlabs) was used for output coupling to a single mode fiber (Corning SMF28), as well as to generate sampling trigger for data acquisition [24].

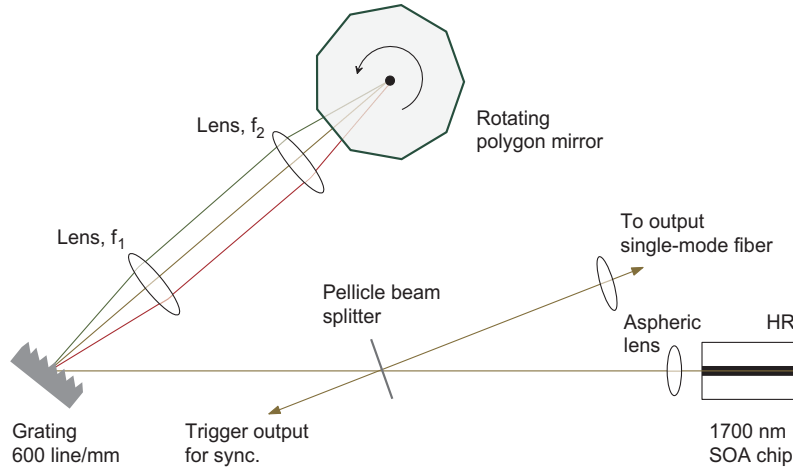


Fig. 1. Experimental setup of the wavelength swept laser in the 1.7- μm spectral range.

Figure 2(a) shows the output spectrum of the swept laser (Design 1). The time-averaged output spectrum spans from 1.59 to 1.75 μm over 160 nm. The instantaneous linewidth was measured to be 0.34 nm, and the average fiber coupled output power was 6.3 mW. The laser could be operated at sweep repetition rates up to 50 kHz. For the spectral measurement, we used a home-built fiber-coupled spectrometer based on a diffraction grating and a calibrated Ge detector (Newport, Model 818-IR). The laser spectrum fits in the valley of optical absorption curve of water, as shown in Fig. 2(b). Low water absorption is desirable for imaging biological samples, which have high water content of typically 70%. We note, however, in most of biological samples optical scattering is a dominant cause of signal attenuation over depth, as evidenced by our experimental results described later in this paper.

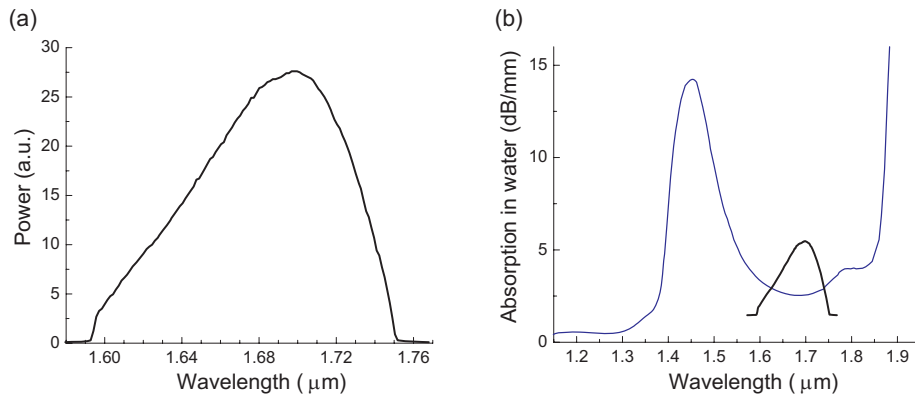


Fig. 2. (a) Output spectrum of the laser in Design 1. (b) Optical absorption curve of water (blue) reported in Ref. [22], superimposed with the laser spectrum (black).

For OFDI, InGaAs detectors are preferred over Ge detectors because of their low noise characteristics. However, the quantum efficiency of a conventional InGaAs detector, as the one used in our OFDI system (New Focus, Model 1817), has a sensitivity roll-off at 1.7 μm . To accommodate this problem, we modified the laser configuration to “Design 2,” matching the tuning range to the high-sensitivity range of the InGaAs detector. Figure 3(a) depicts the output spectrum of the modified laser measured with an optical spectrum analyzer (Agilent) in the peak hold mode. The spectrum spanned from 1.6 to 1.7 μm with a FWHM bandwidth of

64 nm, instantaneous linewidth of 0.21 nm, and the average fiber coupled output power of 12.3 mW. Figure 3(b) depicts a typical time-domain output trace measured with an oscilloscope and the Ge detector when operated at a sweep repetition rate of 10.9 kHz that was used for OFDI imaging.

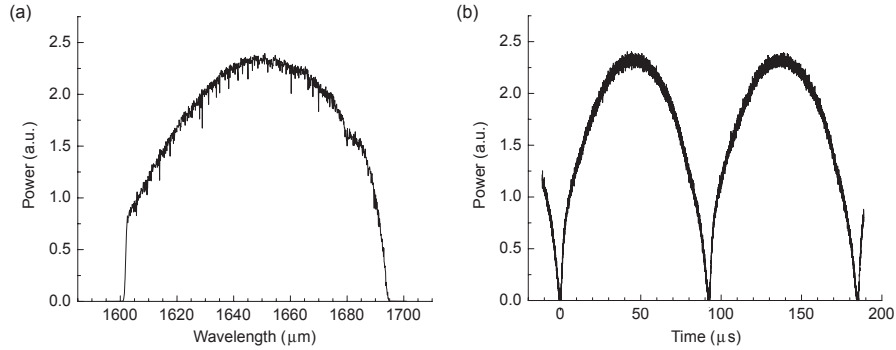


Fig. 3. Measured laser output of Design 2. (a) Peak hold output spectrum. (b) Time domain trace.

2.2 Imaging System: Design and sensitivity analysis

We constructed an OFDI system using the swept laser source. As illustrated in Fig. 4, the system is comprised of a single-mode fiber-optic interferometer (consisting of directional couplers, circulators, and collimators), a galvanometer mirror for beam scanning, detection electronics, and a computer. 80% of the laser output is channeled to the sample arm, while remaining 20% light is directed to the reference arm. The reference arm employs a neutral density (ND) filter to obtain an optimal reference power level. Light returning from the sample and reference arms is combined at a 50/50 coupler and fed to the InGaAs balanced receiver (New Focus 1817). The detector signal is further amplified, low pass filtered (cutoff at 5 MHz), and digitized by a DAQ board (National Instruments, PCI-6115, 12-Bit) at 10 MS/s. Trigger generated from the partial laser output is used to synchronize the data acquisition. A total of 800 data points were acquired during each laser sweep at the A-line rate of 10.9 kHz. The probe beam has a confocal range of 800 μm and a 3-dB full width of 17 μm. Data processing involved reference background subtraction, envelope apodization (windowing), interpolation into linear k-space, and dispersion correction [24].

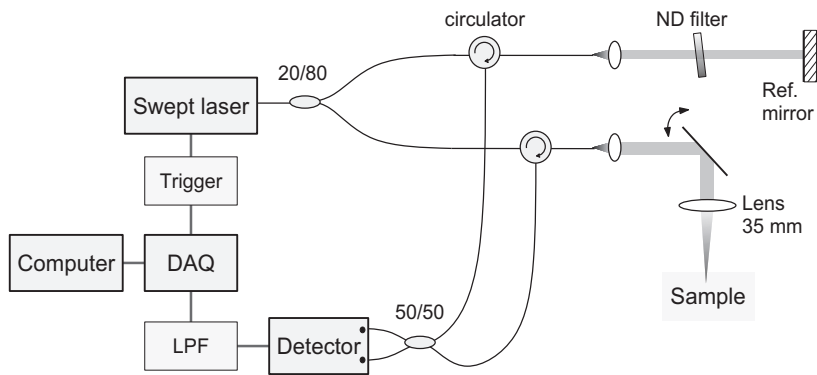


Fig. 4. Schematic of the OFDI system.

We characterized the sensitivity of the system using a partial reflector (-55 dB) with an optimum reference power of 8-12 μW . Figure 5 shows the plot of A-line profile (averaged over 500 measurements incoherently) for the reflector placed at a path length delay (depth) varying from 0.5 mm to 3.5 mm with the optical power on the sample of 7.3 mW. The measured sensitivity was 103 dB at 0.5 mm, which decreases to 100 dB at 1.5 mm and 97 dB at 2.5 mm. We observed an etalon effect due to non-zero reflection from the anti-reflection coated facet of the SOA chip, which resulted in ghost peaks with smaller amplitude at delay differences corresponding to 5.1 mm in air. This artifact, however, is not significant for most turbid samples described later, because the sample power decrease exponentially with depth and thus the ghost artifacts are negligible in the depth range of our interest (up to 3 mm). We observed that the noise floor rose by as much as 5 dB in the presence of relatively high sample powers at large depths; for example, see the increased noise floor due to the partial mirror at 3.5 mm depth (dark yellow curve in Fig. 5). This is attributed to the laser beat noise due to incoherent interference between the sample and secondary (ghost) reference light. This effect, however, did not affect our analysis described in the next section. The measured peak sensitivity near zero delay is about 15 dB lower than the theoretical shot noise limit of 119 dB. Such a discrepancy has been reported previously and attributed to a number of noise sources including imperfect intensity-noise suppression in balanced detection [16,24]. In our system, the discrepancy is thought to be largely due to the wavelength dependent splitting ratio of the fiber couplers that were originally designed for 1.3 μm and the relatively high laser intensity noise due to the etalon effect in the SOA chip, both of which can be improved. Nevertheless, we note that the measured sensitivity in OFDI is substantially higher than the theoretical shot-noise limit of time-domain OCT (92 dB).

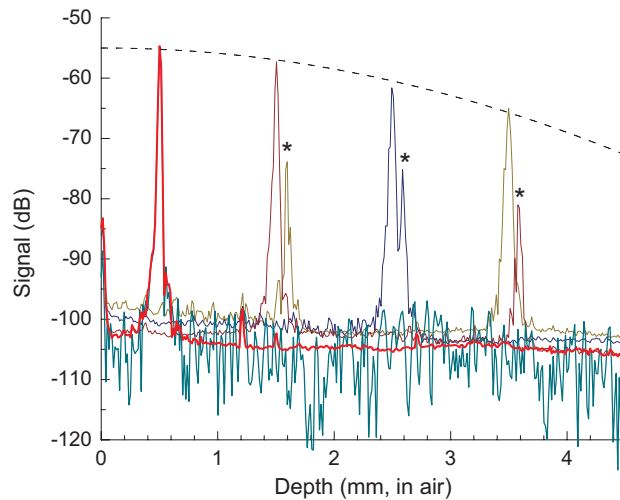


Fig. 5. Signal measured with a -55 dB partial reflector. The detection sensitivity is 103 dB at a depth of 0.5 mm (red) and decreases with the increasing depth (dotted line: a Gaussian fit). A typical single A-line is shown in dark cyan; 500 A-lines at each depth were averaged to reduce the fluctuations in noise floor (red, dark red, navy, and dark yellow). Asterisks (*) denotes the ghost peaks due to the etalon effect of the SOA chip.

3. Methods and analysis

We imaged several biological and phantom samples using the OFDI system at the wavelength (λ) of 1.7 μm . The tested samples were 10% fat emulsion (Intralipid), rubber, human tooth, and skin, which were chosen to evaluate the wavelength-dependent penetration under different scattering and water-induced absorption characteristics. For direct comparison, we imaged the same samples using a state-of-the-art OFDI system previously developed using a swept laser with a tuning range of 1.26 – 1.38 μm [25]. The 1.3 μm OFDI system had a lateral resolution of 12 μm and confocal range of 0.5 mm in the air, whereas the 1.7 μm system had a lateral resolution of 17 μm and a confocal range of 0.8 mm. It is important that the difference in the probe beam parameters does not cause unwanted errors on the analysis described below. To ensure this, the scanning beam waist was positioned at a depth around 1.5 mm in both of the systems. The axial resolution in air was measured to be 24 μm at $\lambda = 1.7 \mu\text{m}$, similar to 20 μm at $\lambda = 1.3 \mu\text{m}$. The detection sensitivity measured at a path length delay of 1.5 mm was 100 dB with the 1.7 μm system and 105 dB with the 1.3 μm system. The sample power was 7.3 mW and 21.3 mW for the 1.7- μm and 1.3- μm systems, respectively. For fair comparison, we added white noise to the raw data obtained with the 1.3 μm system to raise the noise floor by 5 dB. An alternative approach could have been to reduce the sample power by inserting an ND filter with optical density of 0.25 per pass in the sample arm, but we chose not to use this in the experiment to avoid etalon effects by the component.

Single-backscattering model was used in order to extract the total extinction coefficient, μ_t , of the tissues and phantom samples. In a homogenous sample, the backscattered power of the least scattered photons decays exponentially with depth and is given by [26]:

$$P(z) \approx K \mu_b A(z) P_i \exp(-2\mu_t z), \quad (1)$$

where K is a constant, P_i is the incident power to the sample, $A(z)$ is the beam divergence function, μ_b is the backscattering coefficient, and μ_t is the total attenuation coefficient. The effects of incident beam geometry could be neglected as the Rayleigh range is roughly of the same order as penetration depth of ballistic photons. The backscattered power in a dB scale is given by:

$$10 \log_{10}(P(z)) \approx -8.69 \mu_t z + 10 \log_{10}(K \mu_b A P_i) \quad (2)$$

Typical OFDI systems exhibit a drop in sensitivity as a function of the path length difference [24], as also evident in Fig. 5. This depth dependence must be taken into account when measuring the attenuation coefficient from the slope of an A-line profile. In our measurements, a series of A-lines were averaged to reduce the speckle noise (averaging the modulus values after the Fourier transform without subtraction of any offset). Also, the slope of the averaged signal was corrected to subtract the depth dependence of the sensitivity. Regions exhibiting linear decay rates were chosen to calculate the scattering coefficients. This corrected slope is then used to calculate the total extinction coefficient from Eq. (2). The total attenuation coefficient has contributions due to absorption coefficient, μ_a , and scattering coefficient, μ_{sc} ; i.e.

$$\mu_t = \mu_a + \mu_{sc}. \quad (3)$$

In our analysis, the absorption coefficient of a sample was approximated by estimating the absorption due to water content in the sample. The water content value we used was 90% for 10% Intralipid, 70% in the skin, and 0% for other samples. The water absorption coefficient, used in our analysis, is $\sim 0.127 \text{ mm}^{-1}$ and $\sim 0.474 \text{ mm}^{-1}$ at wavelengths of 1.3 μm and 1.7 μm respectively. Our measurement of water absorption at 1.7 μm wavelength yielded a result similar to the reported values [21,22]. In this paper, the scattering and absorption coefficients are defined with the distance unit corresponding to the path length delay in air.

4. Results

4.1 Intralipid sample (10%)

Figure 6(a) and 6(b) show the images of the 10% Intralipid solution obtained with the $1.3\ \mu\text{m}$ and $1.7\ \mu\text{m}$ systems, respectively. It is apparent that the signal penetration is deeper in Fig. 6(b) than 6(a). For quantitative analysis, we averaged 150 A-line scans from the images and plotted the results in Fig. 6(c) and 6(d). The total attenuation coefficients obtained after correcting for the depth-dependent sensitivity were $1.8\ \text{mm}^{-1}$ at $\lambda = 1.3\ \mu\text{m}$ and $1.5\ \text{mm}^{-1}$ at $\lambda = 1.7\ \mu\text{m}$. After subtracting the contribution due to absorption coefficients, the scattering coefficients are found to be $1.7\ \text{mm}^{-1}$ and $1.0\ \text{mm}^{-1}$, respectively.

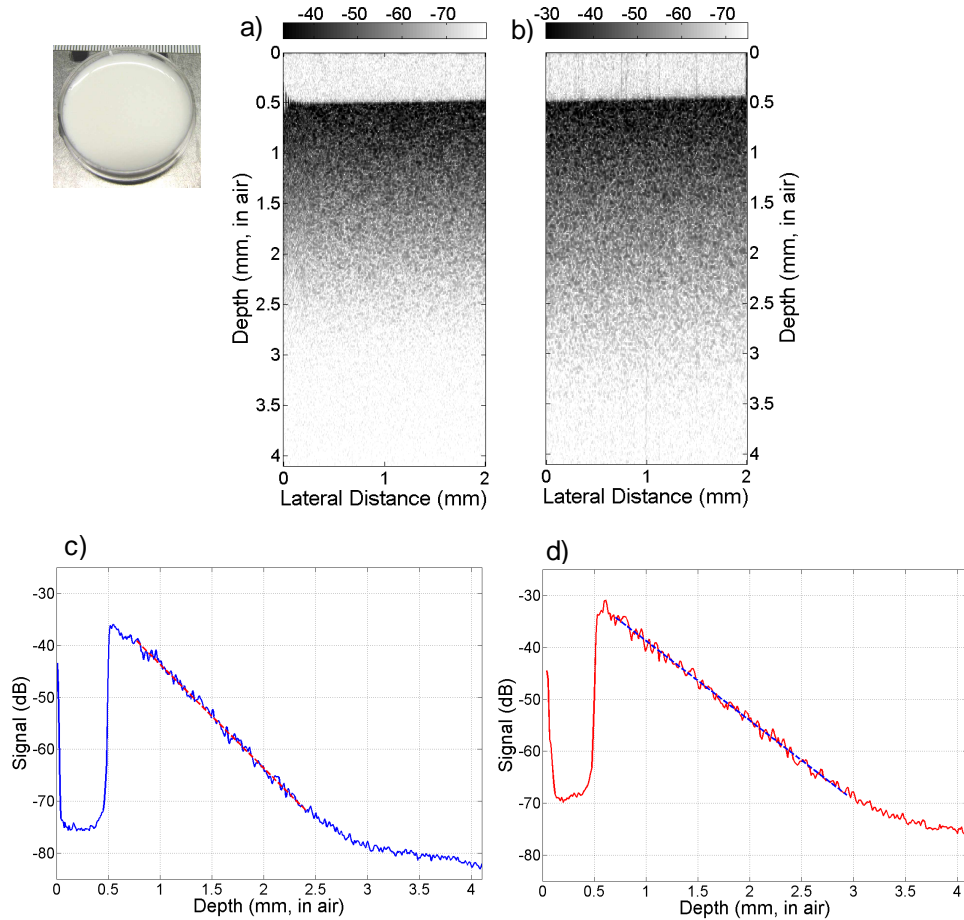


Fig. 6. 10% Intralipid solution. (a,b) OCT images obtained with the $1.3\ \mu\text{m}$ and $1.7\ \mu\text{m}$ systems, respectively. The dynamic range of grayscale is 45 dB, same in both images. (c,d) Depth profiles, averaged over 150 A-lines in (a) and (b), respectively. Dashed lines are linear regressions. The slope was used to determine the total attenuation and scattering coefficients.

4.2 Rubber sample

We tested silicone “red” rubber as a homogenous scattering sample with minimal water content. Signal decrease in rubber showed a marked difference between $1.3\ \mu\text{m}$ and $1.7\ \mu\text{m}$, as evident from the intensity images shown in Fig. 7(a) and (b). Figure 7(c) and (d) depict depth profiles, averaged over 150 A-lines to reduce the speckle. From linear fitting of the slope while neglecting absorption, we measured the scattering coefficient to be $3.5\ \text{mm}^{-1}$ at $\lambda = 1.7\ \mu\text{m}$, which is substantially lower than $5.2\ \text{mm}^{-1}$ measured at $\lambda = 1.3\ \mu\text{m}$. In both images, the depth-dependence of the signal starts to deviate from an exponential decay (linear in dB) at a certain depth. This is probably due to the effect of multiple scattering. The onset of this artifact starts at an axial coordinate of $\sim 1.2\ \text{mm}$ at $\lambda = 1.3\ \mu\text{m}$ [Fig. 7(c)], but this depth is extended to $\sim 1.5\ \text{mm}$ at $\lambda = 1.7\ \mu\text{m}$ [Fig. 7(d)].

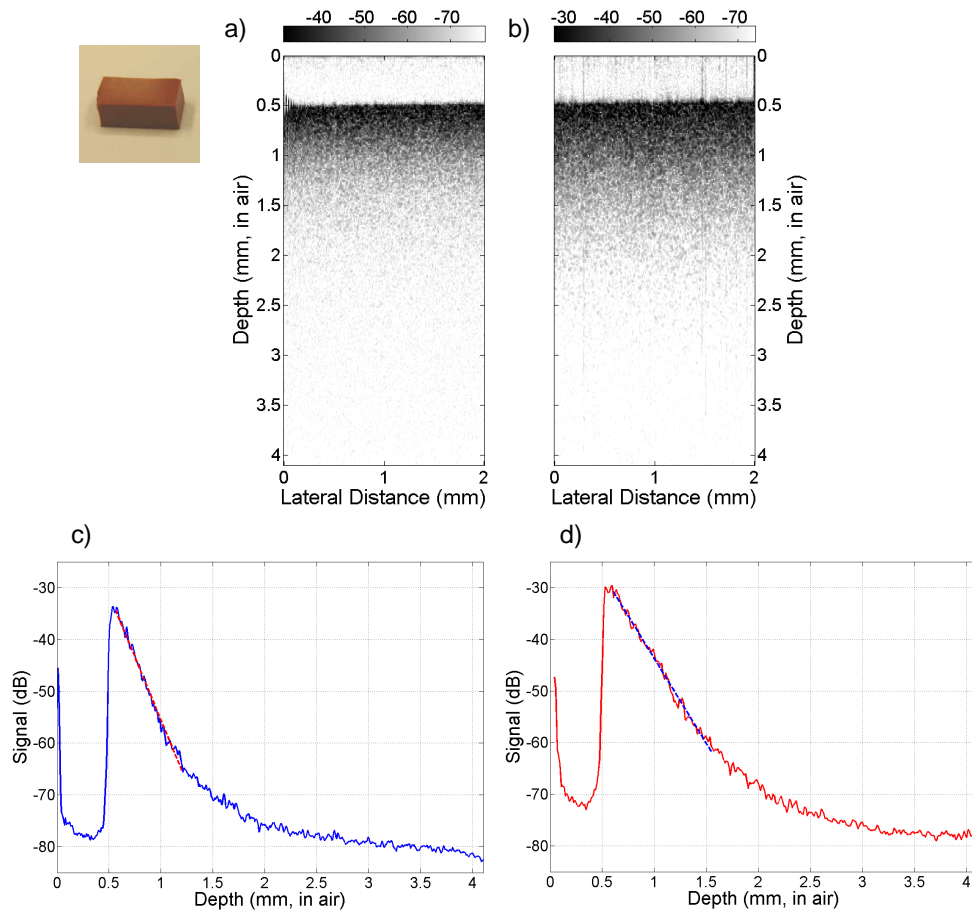


Fig. 7. Silicone red rubber. (a,b) OCT images obtained with the $1.3\ \mu\text{m}$ and $1.7\ \mu\text{m}$ system, respectively. The dynamic range is 47 dB same in both images. (c,d) Depth profiles, averaged over 150 A-lines in (a) and (b), respectively. Dashed line represents linear fit over the region beyond which multiple scattering starts to cause nonlinear dependence on depth.

4.3 Excised human tooth

Figure 8(a) and 8(b) show the cross sectional images of a human tooth sample obtained with the 1.3 μm and 1.7 μm systems, respectively. The enamel-dentin junction can clearly be seen in both images. 50 A-line scans corresponding to the area enclosed between dashed vertical bars are averaged, and the result is shown in Fig. 8(c) and 8(d). The depth profiles show a clear demarcation of two layers with distinctly different attenuation slopes within the enamel, indicating pre and post-natal enamel formation [27]. The scattering coefficients calculated from the depth profiles are 0.8 mm^{-1} and 0.3 mm^{-1} in the pre-natal enamel layer and 0.7 mm^{-1} and 0.8 mm^{-1} in the post-natal enamel layer, at $\lambda = 1.3 \mu\text{m}$ and $1.7 \mu\text{m}$, respectively.

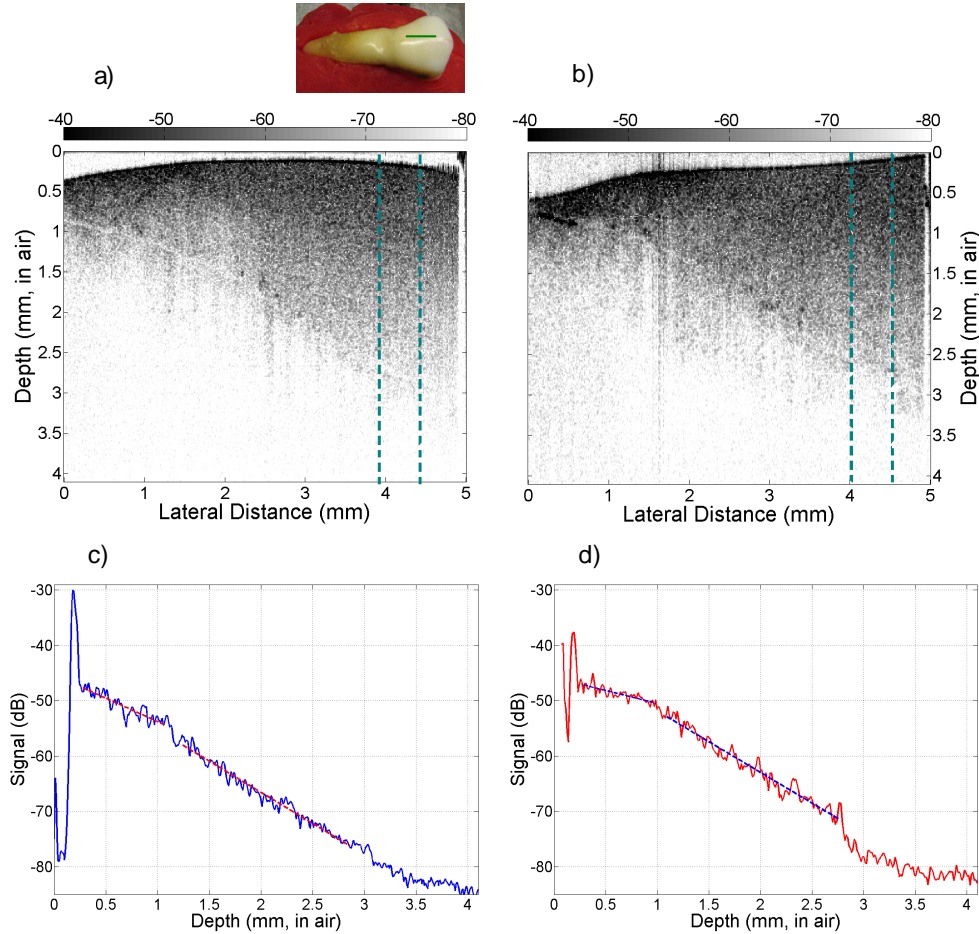


Fig. 8. Human tooth. (a,b) OFDI intensity images obtained (a) with the 1.3 μm system and (b) 1.7 μm system. The grayscale used in both images has the same dynamic range of 40 dB. (c) A-line profile averaged over the area enclosed between dashed vertical bars shown in (a). (d) A-line profile obtained from (b). The slope of the signal decay is distinctly different between the pre- and post-natal regions in the enamel. Inset shows a photograph of the sample where the green line represents the imaged site.

4.4 Human fingertip *in vivo*

Figure 9(a) and 9(b) show the OFDI images of a volunteer's fingertip *in vivo*. A thin slit mask was taped on the finger to ensure that the scan was obtained from approximately the same site. A thin layer of water was applied on the fingertip to reduce specular reflection at the air-skin interface. It appears qualitatively that the penetration depth is slightly improved in the 1.7 μm over 1.3 μm images (e.g. see the contrast near 1.5 mm in depth). Figure 9(c) and 9(d) depict the power average of 85 A-lines in the middle of the images, respectively.

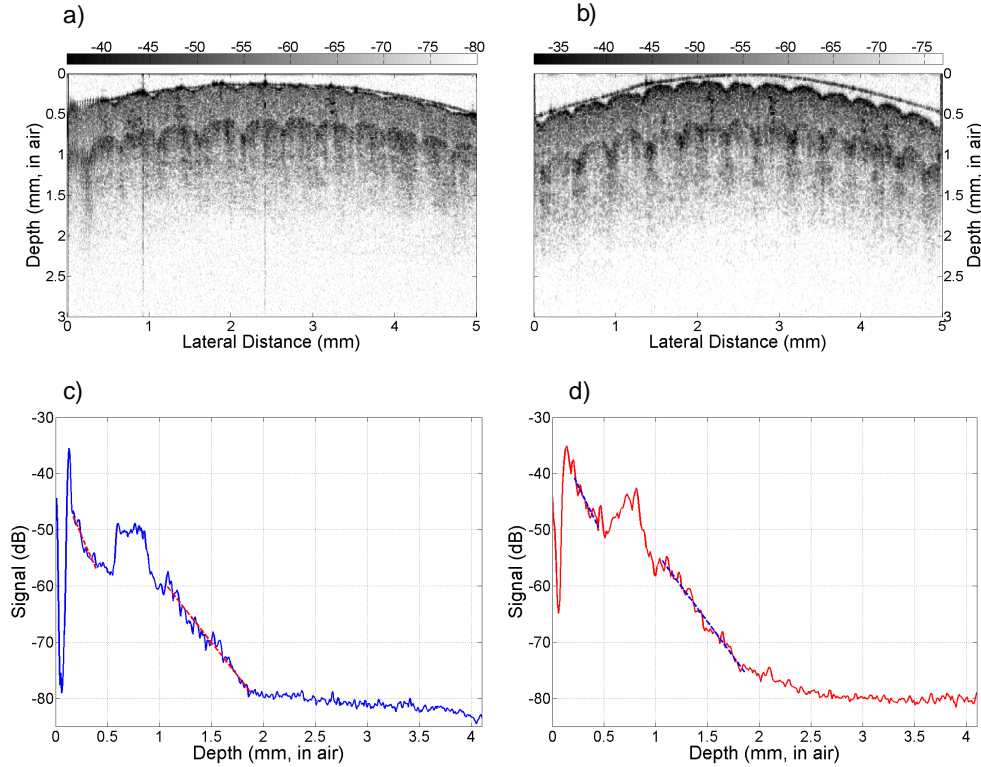


Fig. 9. Human fingertip imaged with (a) 1.3 μm system and (b) 1.7 μm system. The images have the same dynamic range of 40 dB. (c,d) Space-averaged A-line profiles obtained at $\lambda = 1.3 \mu\text{m}$, (c), and 1.7 μm , (d).

4.5 Scattering and attenuation coefficients (Table 1)

Table 1. Comparison of scattering and total attenuation coefficients.

Sample	μ_t (mm^{-1})		μ_a (mm^{-1})		μ_{sc} (mm^{-1})		
	1.3 μm	1.7 μm	1.3 μm	1.7 μm	1.3 μm	1.7 μm	diff.
Intralipid (10%)	1.8	1.45	0.11	0.43	1.7	1.0	-0.7
Rubber	5.2	3.5	0	0	5.2	3.5	-1.7
Enamel (layer1)	0.8	0.3	-	-	0.8	0.3	-0.5
Enamel (layer2)	0.7	0.8	-	-	0.7	0.8	0.1
Epidermis	4.8	4.3	0.09	0.33	4.7	4.0	-0.7
Dermis	2.1	2.4	0.09	0.33	2.0	2.1	0.1

5. Discussion and conclusions

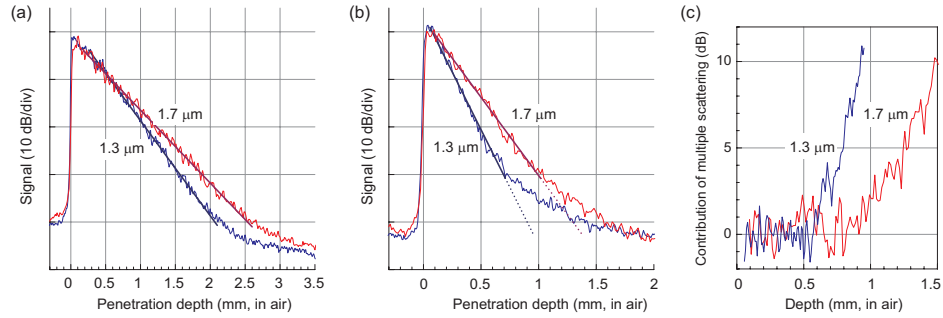


Fig. 10. Enhanced penetration depths at 1.7 μm versus 1.3 μm wavelength. (a) Depth profiles from 10% Intralipid solution (Fig. 6). The ballistic penetration depth is 2.5 mm at $\lambda=1.7 \mu\text{m}$ versus 2.0 mm at $\lambda=1.3 \mu\text{m}$. (b) Depth profiles from silicone rubber (Fig. 7). The ballistic penetration depth is 1.0 mm at $\lambda=1.7 \mu\text{m}$ versus 0.7 mm at $\lambda=1.3 \mu\text{m}$. The ballistic penetration is limited by the onset of multiple scattering marked by the deviation from the linear slope (Lines). (c) The magnitude of multiple-scattering signal estimated by taking the difference of the depth profile from the linear regression in (b).

We have shown that the wavelength region of 1.6 – 1.8 μm is a promising window for OFDI imaging with an advantage of enhanced penetration depth. For most of the tested samples, the slope of signal decay over depth is reduced at 1.7 μm compared to 1.3 μm . The improvement in ballistic penetration was most evident in Intralipid and rubber samples [Fig. 10], although it is less apparent in pre-natal enamel and dermis. Furthermore, we observed that the strength of multiple scattering was reduced considerably at the long wavelength. We point out that the depth in the image, which is the optical delay, assumes the ballistic propagation and so does not correspond to the actual location of the scatterers in the case of multiple scattering. The reduced scattering at 1.7 μm can improve the image contrast at large depths where otherwise the multiply scattered photons may cause artifacts and noise-like background. In addition to these findings, we have demonstrated a wavelength-swept laser and an OFDI system operated in the 1.7- μm region, for the first time to our knowledge. The sensitivity and axial resolution of the 1.7- μm system can be further improved by using low-noise extended InGaAs detectors and better engineered SOA chip. All of the results suggest that 1.7 μm OFDI has the potential to develop into a viable superior technology useful for various applications.

Acknowledgment

This work was supported in part by National Institute Health (Grant R33CA110130) and National Science Foundation (Grant ECCS-0801412). Authors are grateful to M. Suter, B. Vakoc, G. Tearney, and B. Bouma for access to the 1.3- μm system and P. Heim for helpful discussion.